Semiclassical transport and phonon scattering of electrons in semiconducting carbon nanotubes

G. Pennington and N. Goldsman
Department of Electrical Engineering, University of Maryland, College Park, Maryland 20742, USA
(Received 16 July 2002; revised manuscript received 4 November 2002; published 30 July 2003)

Current flow, considering a semiclassical electron–electric-field interaction and electron scattering by acoustic phonons, is studied in semiconducting zig-zag carbon nanotubes. The π-electronic band structure and the phonon spectrum of the nanotube are both calculated from graphene by the zone-folding method. Scattering rates are calculated using first-order perturbation theory and the deformation-potential approximation, while the selection rules for the electron-phonon interaction are developed based on the conservation of crystal momentum. The steady-state transport properties of electrons in small-diameter nanotubes are simulated using the Monte Carlo method. Results show negative differential mobility occurring at smaller threshold fields as the tube diameter increases. The peak drift velocity is also found to depend on the tube diameter, and reaches values as high as 5×10^7 cm/s in the largest tube considered with a diameter of $\cong$4.6 nm. The simulated low-field mobility is as large as in graphite, $\cong 2\times10^4$ cm^2/V/s, for the larger tubes, but decreases as the tube diameter decreases.

DOI: 10.1103/PhysRevB.68.045426 PACS number(s): 73.63.Fg, 72.10.−d

I. INTRODUCTION

Since the discovery[1] of carbon nanotubes (CNT's), interest in the potential applications of their electronic properties has continued to grow. These properties vary with each tube's fundamental indices (n,m), which specify the diameter and wrapping angle as a graphene sheet is seamlessly wrapped into a CNT. As n and m vary, conduction ranges from metallic to semiconducting, with an inverse-diameter-dependent band gap of $\lesssim$1 eV.[2] Furthermore, it has been shown experimentally that different types of CNT's may be seamlessly connected allowing contacts with widely varying conduction properties to be made within the same material.[3,4] Doping of the tubes with donors and acceptors has been demonstrated,[5,6] while metallic tubes have shown the capacity for large current densities and large thermal conductivities.[7,8] These and other versatile electronic properties offer great hope for CNT-based nanoelectronics. Already important steps have been made. A variety of electronic devices operating at room temperature have been produced including field-effect transistors,[9–11] rectifying diodes, and heterojunctions.[12–18] Recently logic circuits using both p and n doped CNT-based FET's (Ref. 9) have shown promising experimental results.

As with conventional electronic devices, theoretical modeling should play a key role in the development of CNT-based electronics by predicting performance at both the device and circuit level. Industrial device modeling is typically performed using ''semiclassical approximations,'' and solving transport equations based on either the drift-diffusion approximation or by solving the Boltzmann's equation. For the latter approach it is common to either solve Boltzmann's equation directly, using an analytical approximation for the distribution function,[19] or indirectly with the Monte Carlo method.[20,21] An intriguing question is in what form can these techniques be used in the modeling of nanoscale devices based on materials such as CNT's. With the advent of the miniaturization of feature lengths in conventional devices to submicron distances, this question is being addressed. It has been found that MOSFET's with inversion layer widths of only a few nanometers, can be simulated using full quantum mechanical treatment along the nanoscale inversion layer potential well only, while maintaining semiclassical transport elsewhere.[22,23] For a CNT, there is nanometer scale confinement along the circumference, but along the tube there are indications that delocalization of π electrons can occur.[24] For long tubes under these conditions, a ''semiclassical treatment'' of electron transport along the tube axis may well be an apt treatment. This is supported by electrical measurements on nanotube transistors and diodes which indicate that semiclassical band-bending models can describe operation at room temperature.[11,18]

Often, the basic properties of the electronic structure and the phonon spectrum of CNT's can be well approximated by the zone-folding method (ZFM).[2] In this method the wrapping of graphene into a CNT imposes restrictions on the available wave vector space, but for allowed wave vectors, the electron and phonon energy spectrum are not altered from that of graphene. The effect of the ZFM on the material properties can be quite significant. For example two-thirds of all CNT's are predicted to be semiconductors, whereas graphene itself is a semimetal. These trends as well as the ZFM results for electronic bandgaps and the density of states in CNT's, have been verified experimentally.[25–27] Since calculations[2,28,29] which go beyond the ZFM, considering the curvature of the CNT, do not significantly improve the portions of the electron and phonon energy spectrum that is relevant in this work, only the ZFM is considered.

Here we focus on a semiclassical charge transport model in semiconducting CNT's based on the ZFM. The internal forces on the electrons are described via quantum mechanics whereas external fields act by altering the electronic crystal momentum via Newtonian mechanics. We consider long and ''perfectly intrinsic'' tubes without deformities, defects, and impurities. Since the bandgap decreases with increasing diameter, we focus on small diameter semiconducting CNT's were the bandgap at room temperature is significantly larger than the thermal energy. A diagram of a $n=10$ single-walled

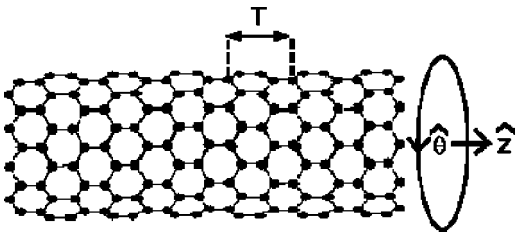

FIG. 1. Zig-zag $n=10$ carbon nanotube, where T is the unit cell length.

CNT is shown in Fig. 1. Along the tube axis, wave vectors are continuous and restricted from the case of graphene due only to the larger length of the CNT unit cell in this direction. Perpendicular to the tube axis although, significant confinement of the electron and phonon eigenvectors allows only discrete wave vector values. The electron is therefore treated as a wave packet of Bloch states along the tube axis but around the tube circumference it is typically delocalized in the small CNT diameters considered here. An analogous treatment for phonons is also used. Electron transport occurs through the action of a uniform electric field directed solely along the tube axis.

Using this semiclassical model, we employ a 1D steady-state Monte Carlo simulation of electron transport along the tube axis of single-walled semiconducting CNT's. Zig-zag tubes, where $m=0$, are considered with wrapping indices of $n=10$ to 59. Since the diameter is proportional to n whereas the bandgap is inversely proportional to n, this corresponds to a diameter range of ≈ 0.8–4.6 nm and a bandgap range of ≈ 1.1–0.1 eV. Transport occurs within electronic subbands obtained from the zone-folded graphene antibonding π-orbital band. Two of the six graphene K point bandstructure valleys are contained within these subbands. Upon scattering with phonons, electrons may make intrasubband, intersubband-intravalley, or intersubband-intervalley transitions. The particular phonon involved depends on selection rules that conserve the total energy and crystal momentum of the electron-phonon system. The crystal momentum is conserved around the circumference as a result of the periodic boundary conditions for both the electrons and phonons. Simulation occurs at low fields, especially in the larger tubes, where acoustic phonon scattering should be important. We observe field controlled negative differential mobility (NDM) caused by the electron transfer between the two lowest energy subbands in the Monte Carlo simulations.

II. ELECTRON AND PHONON ENERGY SPECTRA

As mentioned, both the CNT bandstructure and phonon spectrum are calculated from graphene by the zone-folding method. The CNT Brillouin zone that results is a collection of N 1D slices through the k space of graphene, each with a length of $2\pi/T$, where T is the length of the CNT unit cell and N is the number of graphene unit cells within a single CNT unit cell. For a zig-zag tube of index n, $N=2n$ and $T \approx 0.43$ nm. The Brillouin zone for a $n=10$ zig-zag tube is shown in Fig. 2. It is well known that a metallic CNT is obtained by tube wrappings for which $n-m$ is a multiple of 3.[2] The semiconducting tubes which do not meet this criteria can further be separated into two types, those for which $n-m+1$ is a multiple of 3 and thus a metal and those for which $n-m-1$ would be a metal. These two tube types are distinguished by different trends in the zone-folded electronic energy states near the Fermi level as n and m vary.[30] As shown in Fig. 2, the difference depends on whether the lowest conduction band is obtained right before or right after the zone slices reach the graphene conduction band minimum at the K point.

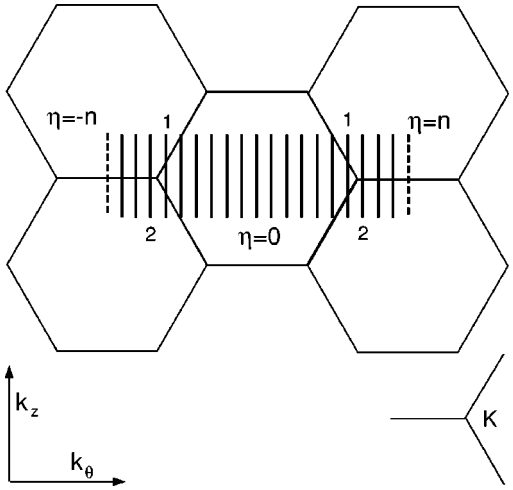

FIG. 2. Brillouin zone for a zig-zag semiconducting CNT superimposed on graphene k space. The example here is for an $n=10$ tube. The wave vector along the tube axis and perpendicular to it are k_z and k_θ, respectively. Two types of semiconductors are possible depending on if slice 1 or slice 2 gives bands closest to the Fermi level. Type 1 is when the greatest common divisor gcd$(n+1,3)=3$ and type 2 is when gcd$(n-1,3)=3$. The 2 dashed lines for $\eta=\pm 10$ are for the zone boundary and count as just one complete slice. The tube type labeling here is distinct from the subband labeling that will be used.

Zone-folding allows just one discrete value for the wave vector perpendicular to the tube axis for each of the $2n$ graphene unit cells within the zig-zag CNT unit cell. The result is that each band of graphene is broken into $2n$ subbands in the nanotube. For a zig-zag tube of diameter d, the electron wave vector is

$$\vec{k}=(k_z,\eta)=k_z\hat{z}+\frac{2\eta}{d}\hat{\theta} \quad (\eta=-n,\ldots,n), \tag{1}$$

where confinement along $\hat{\theta}$ is described by the electronic quantum number η. The wave vectors at $\eta=\pm n$ are treated as one shared zone boundary wave vector. Since we are dealing with long tubes, the z component along the tube axis k_z is treated as continuous. This is equivalent to previous representations of the CNT Brillouin zone where the slices proceed from 0 to $2n-1$,[2] except now symmetry in $\pm\eta$ can be utilized. This is important since, except for the zone boundary value, the electronic subbands are degenerate for $\pm\eta$. There are thus $n+1$ distinct states, $n-1$ of which are doubly degenerate. As seen in Fig. 2, this degeneracy in η corresponds to two equivalent valleys in the subband structure

each centered near a graphene *K* point. It is found that electrons may scatter between and occupy both of these valleys.

As mentioned previously, we consider electron conduction within delocalized π orbitals along the nanotube axis. We therefore are interested in the subbands produced from the π-antibonding band of graphene. This bandstructure is obtained from the π-orbital nearest-neighbor tight-binding bandstructure of a graphene sheet, calculated using a nearest-neighbor π-hopping integral of $\gamma \cong 3$ eV.[2] We do not include the wave function overlap integral. The energy dispersion for a zig-zag tube is

$$E(\vec{k}) = E(k_z, \eta) = \pm \gamma \sqrt{1 \pm 4 \cos\left(\frac{Tk_z}{2}\right)\cos\left(\frac{\pi\eta}{n}\right) + 4\cos^2\left(\frac{\pi\eta}{n}\right)} \quad \left(-\frac{\pi}{T} < k_z < \frac{\pi}{T}\right). \tag{2}$$

Results agree with experimentally measured band gap energies and density of states in CNT's.[25,26] The conduction electron wave function, consistent with the zone-folding method, is

$$\psi_{\vec{k}} = \sum_{\vec{k}} \langle \vec{r} | \vec{k} \rangle = \frac{1}{\sqrt{2\pi L}} \sum_{k_z \eta} e^{i(k_z z + \eta\theta)} u_{k_z \eta}(z, \theta), \tag{3}$$

where L is the CNT length and u are the graphene π-antibonding orbitals that are normalized over the graphene unit cell. Since we are interested electron transport at relatively low applied fields, we focus on the electron bandstructure of the first few subbands. The energy $E_b(k_z)$ of the first three of these subbands, labeled by the subband index b, is modeled using the following analytical expression:

$$\frac{\hbar^2 k_z^2}{2m_b^*(n)} = [E_b - E_b^m(n)]\{1 + \alpha_b(n)[E_b - E_b^m(n)]\} \quad (b = 1,2,3). \tag{4}$$

Here $E_b^m(n)$, $m_b^*(n)$, and $\alpha_b(n)$ are the energy minimum, effective mass, and nonparabolicity factor of subband b respectively. In Table I, each is given as a function of the fundamental tube index n or equivalently, since $d \propto n$, as a function of diameter d. The subband quantum numbers, $\eta_b(n)$ in Table I, are also n dependent. For low-field transport in the first few subbands, it is desirable that this energy model be accurate for electron energies up to $5E_1^m$ above the Fermi level, where the Fermi level is located halfway between the conduction and valence subbands. In this range, the subband energy model reproduces the tight-binding bandstructure with percent error of less than 2%. Considering just the bandstructure near the Fermi level is a good approximation since at equilibrium a conduction electron is over 10 million more times likely to occupy the first subband minimum than an energy as high as $5E_1^m$. The bandstructure of zig-zag semiconductors with $n = 10$ and $n = 59$ are shown in Fig. 3, representing the n index range of the simulations. This range is chosen since the energy separation between the first two subbands is much larger than the thermal energy, allowing the relative population of these subbands to be controlled by the external field.

The phonon wave vector $\vec{q} = (q_z, \eta_p)$ also takes the form of Eq. (1). Similarly to the electron, the axial component q_z is continuous and the phonon is localized as a wave packet along this direction. In the high-symmetry achiral zig-zag tubes that we focus on, the presence of mirror planes allows the phonon eigenvectors to generally fall into longitudinal and transverse polarizations.[31] A torsional polarization is also possible in a CNT. For the phonon energy spectrum of graphene we use a fourth-nearest-neighbor force constant model. Force parameters are used which have been successfully fitted to experiments.[2] Similarly to the electronic energy bands, zone-folding splits up each of the 6 phonon branches of graphene into $2n$ subbranches in the nanotube, each specified by a subbranch quantum number η_p.

In this work the CNT subbranches of the graphene acoustic modes are considered. Of these phonons, there are four for which the phonon energy E_p vanishes as the wave vector q_z vanishes. These include a longitudinal, torsional, and a doubly degenerate transverse mode. Once the electron-phonon scattering selection rules are determined in the next section, its found that these four phonons are involved in only intraband-intravalley electron transitions. This results since each of these modes has a subbranch quantum number of zero, and thus has no wavevector component perpendicular to the tube axis. Due to the quantization of the wavevector along the circumference, most of the CNT acoustic modes have a dispersion relation in which the phonon energy is nonzero as $q_z \to 0$. These subbranches all have a nonzero η_p and turn out to be involved in intersubband electron scattering. Those with a large η_p mediate intervalley scattering.

Since theory predicts that the change in the π-electronic energy under longitudinal strain is larger than under torsional[32,33] or transverse[34] strain, electron scattering by longitudinal polarizations is treated as the most dominant of the acoustic modes. The importance of these longitudinal modes has been observed in thermal relaxation studies of nanotubes.[35] We therefore consider just the longitudinal acoustic modes. For scattering of electrons within the first three conduction bands, the spectra of the acoustic phonons considered is shown in Fig. 4. The energy dispersion relation is

$$E_p(q_z, \eta_p) = E_p^o(\eta_p) + \hbar v_s \Theta(q_z, \eta_p)\left(|q_z| - \left|\frac{\eta_p}{d}\right|\right), \tag{5}$$

were $v_s = 20$ km/s and the phonon energies at $q_z = 0$, $E_p^o(\eta_p)$, are given in Table II. For the *LA-IV* phonon $\Theta = 0$, whereas for the other acoustic modes

$$\Theta(q_z, \eta_p) = \begin{cases} 1 & |q_z| > \left|\dfrac{\eta_p}{d}\right|, \\ 0 & \text{else.} \end{cases} \tag{6}$$

As the tube diameter increases the intravalley phonons all converge to the graphene longitudinal acoustic phonon. The

TABLE I. Band-structure properties. Here n is the fundamental tube index of a zig-zag CNT, γ is the tight-binding hopping integral, E^m are the subband minima in eV, m^* are the subband effective masses, α are the subband nonparabolic factors, and η are the subband quantum numbers. Also η_0 is $2n/3$ rounded to the nearest integer and $\gcd(x,y)$ is the greatest common divisor of x and y.

Subband 1

$$E_1^m(n)=\frac{\pi\gamma}{\sqrt{3}n},$$
$$m_1^*(n)=\frac{3m_e}{n\gamma}\left(1-0.0044n+\frac{\gcd(n+1,3)-\gcd(n-1,3)}{n}\right),$$
$$\alpha_1(n)=\frac{3}{2\gamma}(0.3n-1),$$
$$\eta_1(n)=\pm\eta_0.$$

Subband 2

$$E_2^m(n)=2E_1^m(n)\left(1+\frac{\gcd(n-1,3)-\gcd(n+1,3)}{3n}\right),$$
$$m_2^*(n)=m_1^*(n)\left(\frac{E_2^m(n)}{E_1^m(n)}+\frac{5}{n}\left[\frac{E_2^m(n)}{E_1^m(n)}[\gcd(n-1,3)-1]-[\gcd(n+1,3)-1]\right]\right),$$
$$\alpha_2(n)=\frac{3}{2\gamma}(0.2n-1),$$
$$\eta_2(n)=\pm 2(n-\eta_0).$$

Subband 3

$$E_3^m(n)=4E_1^m(n)\left(1+\frac{1+2\gcd(n+1,3)-3\gcd(n-1,3)}{4n}\right),$$
$$m_3^*(n)=m_1^*(n)\left(\frac{E_3^m(n)}{E_1^m(n)}+\frac{5}{n}\left[\frac{E_3^m(n)}{E_1^m(n)}[\gcd(n+1,3)-1]-[\gcd(n-1,3)-1]\right]\right),$$
$$\alpha_3(n)=\frac{3n^2}{300\gamma},$$
$$\eta_3(n)=\pm 2(2\eta_0-n).$$

intervalley subbranches, grouped together as *LA-IV* in Fig. 4, are to a good approximation dispersionless with an energy of $\cong 160$ meV. An exception though is the intervalley acoustic phonon that scatters electrons between the third subband of different valleys. This phonon has less energy, but as the tube diameter increases, its energy also approachs 160 meV.

III. ELECTRON-PHONON SCATTERING

Electron-phonon scattering in CNT's is treated using the standard methods of lattice scattering.[36] The effect of ion vibrations on the periodic crystal potential is considered small enough to treat using first-order perturbation theory. Considering the duration of a scattering event to be short, the rate of electron-phonon scattering is represented by the familiar golden rule

$$\Gamma=\frac{2\pi}{\hbar}|\langle f|H^{ep}|i\rangle|^2\delta(E_f-E_i), \tag{7}$$

where i and f are the initial and final states of the system, E is the energy, and H^{ep} is the space-dependent electron-phonon interaction. Assuming short-range interactions we will use the deformation theory[37] to approximate H^{ep}. Using longitudinally polarized phonon eigenvectors in a form consistent with confinement in the ZFM, the displacement of the lattice at a tube position of $\vec{r}=z\hat{z}+(\theta d/2)\hat{\theta}$ is

$$U(\vec{r})=\sum_{\vec{q}}\sqrt{\frac{\hbar}{2M\omega_{\vec{q}}}}[a_{\vec{q}}e^{i(\vec{q}\cdot\vec{r})}\hat{q}+\text{c.c.}]. \tag{8}$$

The sum is over phonon wave vectors $\vec{q}=q_z\hat{z}+(2\eta_p/d)\hat{\theta}$, where z and θ are the coordinates along the tube axis and around the tube circumference respectively. As mentioned the component of the wave vector along the tube q_z is treated as continuous since the tube length is large, whereas the

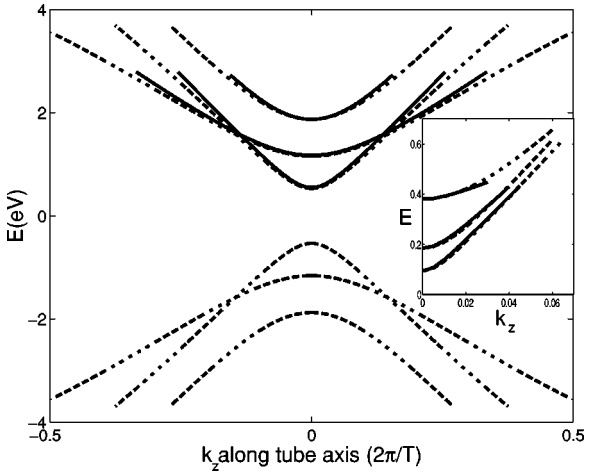

FIG. 3. Band-structure for a $n=10$ zig-zag CNT. Tight-binding band-structure (dash line) and the model subbands (solid line) of Eq. (4) are shown. The inset is for a $n=59$ tube. These represent the range of CNT sizes simulated in this work.

component along θ is quantized. So the sum includes all subbranches η_p. The amplitude of each eigenvector depends on the lattice mass M, the subbranch wave-vector-dependent frequency $\omega_{\vec{q}}$, and the phonon creation and anniliation operators $a^\dagger$ and a. The electron-phonon interaction H^{ep} is found from the shift in electronic energy due to a phonon. Within the deformation potential theory, this shift is given by the perturbation of the electronic energy when an electron interacts with a long wavelength phonon and is set equivalent to the effect of a locally homogeneous strain. This electronic energy change is then

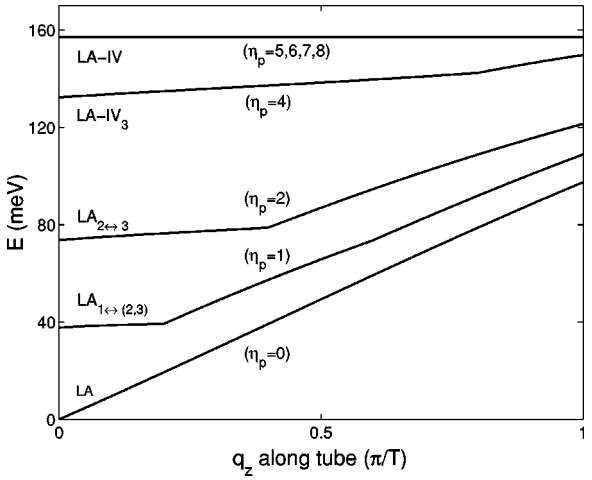

FIG. 4. Carbon nanotube phonon dispersion for a $n=10$ zig-zag tube. For the intravalley processes there are the longitudinal acoustic modes (*LA*), which are separated based on the subband transitions they are involved in. The intervalley phonons are grouped as (*LA-IV*) since they have approximately the same energy. The intervalley phonon for transitions between the third subband of each valley, (LA-IV_3), is an exception with lower energy.

$$\langle \vec{k}'|\Delta E|\vec{k}\rangle = \langle \vec{k}'|D\sum_{\vec{q}} \sqrt{\frac{\hbar}{2M\omega_{\vec{q}}}}[iqa_{\vec{q}}e^{i(\vec{q}\cdot\vec{r})}+\text{c.c.}]|\vec{k}\rangle$$

$$= D\sum_{q_z\eta_p} \sqrt{\frac{\hbar\left[q_z^2+\left(\frac{2\eta_p}{d}\right)^2\right]}{2M\omega_{q_z\eta_p}}} \times\langle \vec{k}'|ia_{q_z\eta_p}e^{i(q_z z+\eta_p\theta)}+\text{c.c.}|\vec{k}\rangle, \quad (9)$$

for an electron transition from state $\vec{k}$ to state $\vec{k}'$. The deformation potential D is the proportionality constant between the electronic energy shift and the lattice strain. For zig-zag tubes, D has been calculated to be approximately 3γ.[32,34]

Now we concentrate on the matrix elements that determine the electron-phonon selection rules. Using the electron wave function in Eq. (3) and the lattice symmetry along the tube axis the following matrix element becomes

$$\langle \vec{k}'|e^{i(q_z z+\eta_p\theta)}|\vec{k}\rangle = \frac{N_T\delta_{k_z-k_z',q_z}}{2\pi L} \times\int_0^T dz\int_0^{2\pi} d\theta e^{i\delta\eta\theta}u^*_{\vec{k}'}(z,\theta)u_{\vec{k}}(z,\theta), \quad (10)$$

where $\delta\eta=\eta-\eta'+\eta_p$. Here the integral along the entire tube is replaced by the integral along just the CNT unit cell by using the axial-symmetry relations

$$\sum_{j=1}^{j=N_T} e^{i(k_z-k_z'+q_z)jT}=N_T\delta_{k_z-k_z',q_z} \quad (11)$$

and

$$u_{\vec{k}}(z+jT,\theta)=u_{\vec{k}}(z,\theta), \quad (12)$$

where jT are the lattice vectors along z and N_T is the total number of CNT unit cells in the tube.

Now using the CNT symmetry vector[2] for a zig-zag tube $\vec{R}$ the positions of each graphene unit cell can be found according to

$$\alpha\vec{R}=\alpha\left[\frac{T}{2}\hat{z}+\frac{\pi d}{N}\hat{\theta}\right], \quad \alpha=\text{integers } (1,\ldots,N). \quad (13)$$

The z component of $\alpha\vec{R}$ wraps back around so that it always stays within the unit cell, which has a of length T along the z direction. This is shown in Fig. 5(a). The unit cell can be redrawn as in Fig. 5(b), so that the integration along z is now continuous. Then Eq. (9) may be written as

TABLE II. Phonon properties. Here n is the fundamental tube index of a zig-zag CNT, γ is the tight-binding hopping integral in (eV), and η_p are the subbranch quantum numbers. Also η_0 is $2n/3$ rounded to the nearest integer and $E_p^o[\eta_p(n)]$ is the phonon energy at $q_z=0$. Intravalley modes show linear dispersion with a characteristic velocity of $v_s=20$ km/s.

Phonon	Band transfer	$E_p^o(\eta_p)$ (eV)	$\eta_p(n)$
LA	intrasubband-intravalley	0	0
$LA_{1\leftrightarrow(2,3)}$	intersubband-intravalley $1\leftrightarrow(2,3)$	$\frac{3}{8n}$	± 1
$LA_{2\leftrightarrow 3}$	intersubband-intravalley $2\leftrightarrow 3$	$\frac{3}{4n}$	± 2
$LA-IV$	intersubband-intervalley $1\leftrightarrow 1$	0.160	$\pm 2(n-\eta_0)$
$LA-IV$	intersubband-intervalley $2\leftrightarrow 2$	0.160	$\pm 2(2\eta_0-n)$
$LA-IV_3$	intersubband-intervalley $3\leftrightarrow 3$	$0.160\left(1-\frac{10}{n^2}\right)$	$\pm 2(3n-4\eta_0)$
$LA-IV$	intersubband-intervalley $1\leftrightarrow 2$	0.160	$\pm\eta_0$
$LA-IV$	intersubband-intervalley $1\leftrightarrow 3$	0.160	$\pm(4n-5\eta_0)$
$LA-IV$	intersubband-intervalley $2\leftrightarrow 3$	0.160	$\pm 2(n-\eta_0)$

$$\langle \vec{k}'|e^{i(q_z z+\eta_p\theta)}|\vec{k}\rangle = \frac{N_T\delta_{k_z-k_z',q_z}}{2\pi L} \times \sum_{\alpha=1}^{\alpha=N}\int_{T(\alpha-1)/2}^{T\alpha/2} dz \int_{2\pi(2z-T)/TN}^{2\pi(2z+T)/TN} d\theta e^{i\delta\eta\theta} u_{\vec{k}'}^*(z,\theta) \times u_{\vec{k}}(z,\theta). \quad (14)$$

Now using the $\vec{R}$ symmetry of the graphene unit cells, which are contained within the CNT unit cell

$$u_{\vec{k}}(\vec{r}+\alpha\vec{R}) = u_{\vec{k}}(\vec{r}), \quad (15)$$

Eq. (14) may be reduced to a integration over a single graphene unit cell

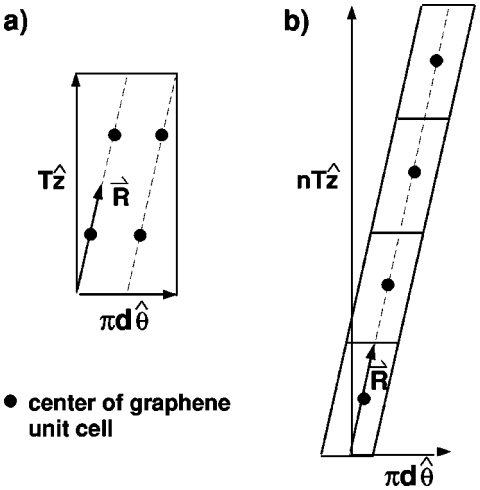

FIG. 5. (a) Unit cell for a $(n,m)=(2,0)$ CNT. Four graphene unit cells are contained and located at multiples of the wrapped symmetry vector $\vec{R}$. (b) Unwrapped CNT unit cell.

$$\langle \vec{k}'|e^{i(qz+\eta_p\theta)}|\vec{k}\rangle = \frac{N_T\delta_{k_z-k_z',q_z}}{2\pi L} \times \int_0^{T/2} dz \int_{4\pi(z-T)/TN}^{4\pi z/TN} d\theta e^{i\delta\eta\theta} \times u_{\vec{k}'}^*(z,\theta)u_{\vec{k}}(z,\theta)\sum_{\alpha=1}^{\alpha=N} e^{i\delta\eta(2\pi\alpha/N)}. \quad (16)$$

Since there is periodicity around the circumference, the sum may be equivalently redrawn by starting the sum at an arbitrary graphene unit cell $\beta+1$, where β is an integer

$$\sum_{\alpha=1}^{\alpha=N} e^{i\delta\eta(2\pi\alpha/N)} = \sum_{\alpha=\beta+1}^{\alpha=\beta+N} e^{i\delta\eta(2\pi\alpha/N)} = e^{i\delta\eta(2\pi\beta/N)}\sum_{\alpha=1}^{\alpha=N} e^{i\delta\eta(2\pi\alpha/N)}. \quad (17)$$

To satisfy this condition for arbitrary β, $\delta\eta$ must be zero and thus

$$\sum_{\alpha=1}^{\alpha=N} e^{i\delta\eta(2\pi\alpha/N)} = N\delta_{\delta\eta,0} = N\delta_{\eta'-\eta,\eta_p}. \quad (18)$$

This gives

$$\langle \vec{k}'|e^{i(qz+\eta_p\theta)}|\vec{k}\rangle = \frac{NN_T\delta_{k_z-k_z',q_z}\delta_{\eta'-\eta,\eta_p}}{2\pi L} \times \int_0^{T/2} dz \int_{4\pi(z-T)/TN}^{4\pi z/TN} d\theta u_{\vec{k}'}^*(z,\theta)u_{\vec{k}}(z,\theta) = \delta_{k_z-k_z',q_z}\delta_{\eta'-\eta,\eta_p}, \quad (19)$$

since the graphene π-antibonding orbitals are normalized over the graphene unit cell.

These are the selection rules for phonons involved in a given transition from an initial $\vec{k}=(k_z,\eta)$ to a final $\vec{k}'=(k_z',\eta')$ electron state. Electron-phonon scattering must not only conserve momentum along the tube axis but also conserve the quantum number η. The periodic boundary conditions for the electrons and phonons along the circumference retain the conservation of the 2D crystal momentum in the CNT's. The electron-phonon interaction is

$$|\langle f|H^{ep}|i\rangle|^2 = |\langle \vec{k}';N(\pm)1|\Delta E|\vec{k};N\rangle|^2 = \sum_{q_z^*\eta_p^*} \frac{\hbar^2 D^2\left[q_z^2+\left(\frac{2\eta_p}{d}\right)^2\right]\left[N(q_z,\eta_p)+\frac{1}{2}(\pm)\frac{1}{2}\right]}{2ME_p(q_z,\eta_p)}, \tag{20}$$

where the sum includes all phonon wave vectors q_z^* and quantum numbers η_p^* that satisfy the selection rules in Eq. (19). N is the phonon occupation number represented using the Bose-Einstein distribution function, while in the bracketed $(\pm)$ sign, the upper sign is for phonon emission and the lower for phonon absorption.

Using Eq. (7) the golden rule and integrating over all final electron states, the scattering rate from an electronic state in subband b with wavevecter k_z to an electronic state in subband b' is

$$\Gamma_{bb'}(k_z) = \sum_{q_z^*\eta_p^*} \frac{\hbar D^2\left[q_z^2+\left(\frac{2\eta_p}{d}\right)^2\right]}{2\rho E_p(q_z,\eta_p)} \times\left(N[E_p(q_z,\eta_p)]+\frac{1}{2}(\pm)\frac{1}{2}\right) I_{bb'}(k_z,q_z,\eta_p), \tag{21}$$

where ρ is the CNT mass density along the tube axis and conservation of energy and crystal momentum is also required. The term $I_{bb'}$ would typically correspond to a function of the density of final states under the golden rule formalism. Since semiclassically the density of states diverges in 1D, higher order quantum effects are needed. It has been found in quantum wires that a full quantum mechanical treatment of the 1D scattering rate can be well approximated by including collisional broadening within the golden rule.[38,39] Following these results we adjust Eq. (21) by broadening the semiclassical $I_{bb'}$ with a Gaussian according to

$$I_{bb'}(k_z,q_z,\eta_p) = \frac{\sqrt{2/\pi}}{\Delta[1+\mathrm{erf}(E)]} \times\int_{-E}^{\infty} \frac{e^{-(E'^2/2\Delta^2)}\mathrm{DOS}_{b'}(E+E')dE'}{1(\pm)\frac{q_z}{|q_z|}\hbar v_s\Theta(E_p+E')\mathrm{DOS}_{b'}(E+E')}, \tag{22}$$

where $\mathrm{DOS}_{b'}$ is the density of states in band b', erf is the error function, and

$$E=E_b(k_z)(\mp)E_p(q_z,\eta_p). \tag{23}$$

The broadening of final states Δ is determined self-consistently for each member of the sum in Eq. (21) according to

$$\Delta=\hbar\Gamma_{bb'}(k_z,q_z,\eta_p). \tag{24}$$

When b and b' correspond to different valleys in the electronic subband structure, η_p is large. These intervalley phonons, grouped as *LA-IV*, have the same phonon energy, but since they cause different subband electron transitions and therefore have different quantum numbers η_p, they will have different scattering rates. As previously mentioned and given in Eqs. (5) and (6), the phonon energy dispersion is significant for the intravalley subbranches with small η_p. For the *LA* intrasubband branch when E_p is much less than the thermal energy K_bT_L, only backscattering occurs and we use the small phonon energy limit[36]

$$\frac{q_z^{*2}\left\{N[E_p(q_z^*)]+\frac{1}{2}(\pm)\frac{1}{2}\right\}}{Ep(q_z^*)} \cong \frac{K_bT_L}{\hbar^2 v_s^2}, \tag{25}$$

in Eq. (21).

In Fig. 6 the room temperature scattering rates, are shown for electrons in the first two subbands of a $n=10$ and $n=59$ zig-zag CNT. Both the total longitudinal acoustic intravalley and intervalley scattering are shown. Since the scattering rate depends on the density of final electron states, the $1D$ scattering rate peaks when electrons can scatter into states near a subband minima. This can be readily seen in the peaks of Fig. 6. The scattering rates are seen to markedly decrease as n and thus the tube diameter increases. This occurs since with increasing diameter the density of final scattering states decreases and the CNT mass per unit length increases, both decreasing the scattering rate. It is found that the rates decrease by roughly an order of magnitude as n progresses from $10\rightarrow 59$. At room temperature, electron scattering by absorption of intervalley phonons is weak, but this should not be the case for much larger temperatures. Conversely, for the intravalley phonons with low energies, the absorption and emission scattering rates are nearly the same.

The dominant scattering mechanisms, once the electron energy reaches a required phonon emission threshold, are the intervalley process. After the onset of these stronger events, intravalley scattering does not contribute significantly to the total rate, except near the peaks indicated in Fig. 6. These peaks usually correspond to an absorption peak closely followed by and emission peak. At low energies near the subband minimum, before the onset of the intervalley events, the character of the scattering varies with tube size. Here intrasubband-intravalley scattering is strong but other mechanisms also contribute. In large tubes electrons in subband 1 are scattered significantly by intravalley $(1\rightarrow 2)$ phonon emission and absorption processes at low energies. This is not seen in the smaller tubes since before the electron can

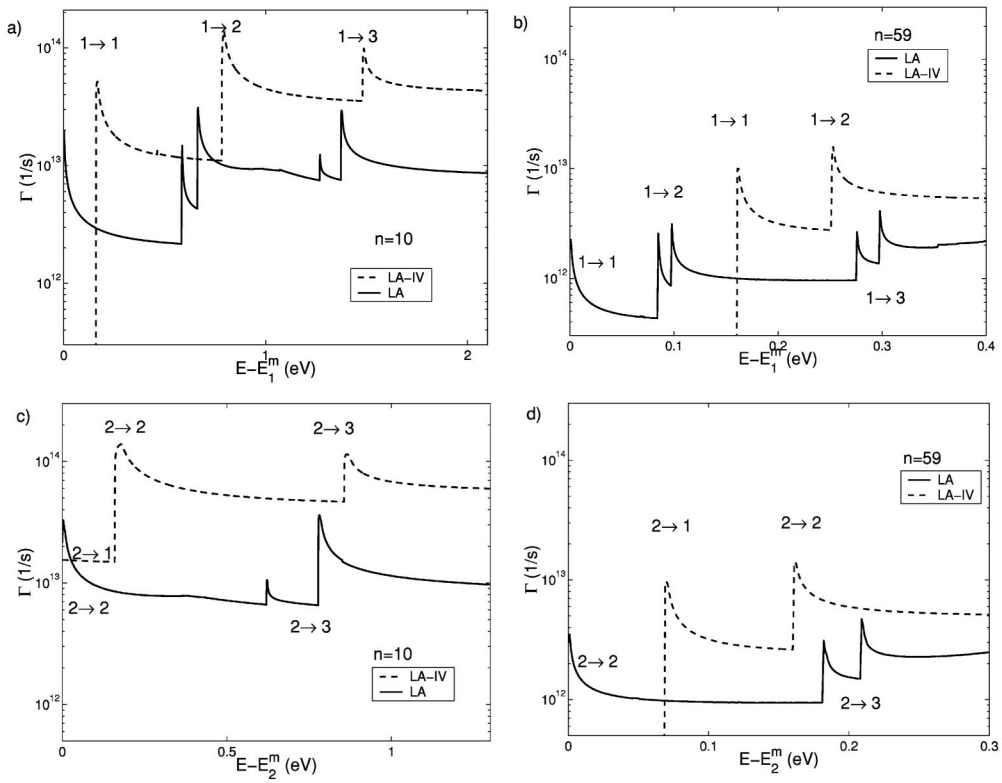

FIG. 6. Room temperature scattering rate Γ as a function of electron energy for (a) electron in band 1 of an $n=10$ tube, (b) electron in band 1 of an $n=59$ tube, (c) electron in band 2 of an $n=10$ tube, and (d) electron in band 2 of an $n=59$ tube. The total longitudinal acoustic intravalley (*LA*) and intervalley (*LA-IV*) scattering rates are shown. The peaks in the intervalley rate are all due to phonon emission. Intervalley absorption is rare since the large phonon energies limit the population of thermally excited phonons at room temperature. In the intravalley rate with lower phonon energies, an absorption followed closely by an emission peak are shown for each electronic subband transition. The phonons involved are given in Table II.

reach energies to allow these intravalley $(1\rightarrow 2)$ processes, the threshold at 160 meV for the strong $(1\rightarrow 1)$ intervalley process is reached. For electrons in subband 2 of the small tubes, near the energy minimum, strong $(2\rightarrow 1)$ intervalley phonon emission processes occurs. In the larger tubes, the energy gap between the subbands is too small and only the intravalley $(2\rightarrow 2)$ process occurs.

IV. TRANSPORT SIMULATION

Charge transport in zig-zag semiconducting CNT's is studied using standard Monte Carlo techniques.[20] Simulations are homogeneous and of sufficient time duration to characterize steady-state phenomena of many noninteracting electrons using the single-electron method.[20] CNT's are treated as ''ideal,'' in that they are extremely long, undoped, and without any defects or other imperfections. The basic principles of semiclassical transport[40] are used, in which quantum mechanics is used to determine the electronic energy levels and scattering rates due to the lattice, whereas applied external fields accelerate electrons semiclassically. In this work a homogeneous external electric field directed solely along the CNT axis is considered. This field is not considered strong enough to cause intersubband transitions in the CNTs simulated. The validity of this approximation requires that the subband separation ΔE always obey the relation[40]

$$\Delta E > \sqrt{E_F e F T}, \tag{26}$$

where E_F is the Fermi energy of graphene, e is the electron charge, F is the external electric field, and T the magnitude of the translation vector. An obvious exception occurs in the smaller diameter tubes where subband crossing occurs. This can be seen in Fig. 2. For simplicity in this work, the consequences of subband crossing are ignored.

As mentioned, the only scattering mechanism considered involves the subbranches of the graphene longitudinal acoustic mode. Electron-electron scattering is not included here but may contribute to the electron drift velocity by increasing the intersubband-intervalley scattering rate. This would be more likely in the larger tubes we consider, where both the transverse momentum transfer between the subbands and the phonon scattering rate are small. Intrasubband scattering via electron-electron interactions though should not effect the electron drift velocity since the initial and final interacting electron pair would be indistinguishable in one dimension, leading to no net randomization of the net electron momentum of the system.[41]

It is necessary to point out that in one dimension the Monte Carlo simulation is complicated by peaks in the scat-

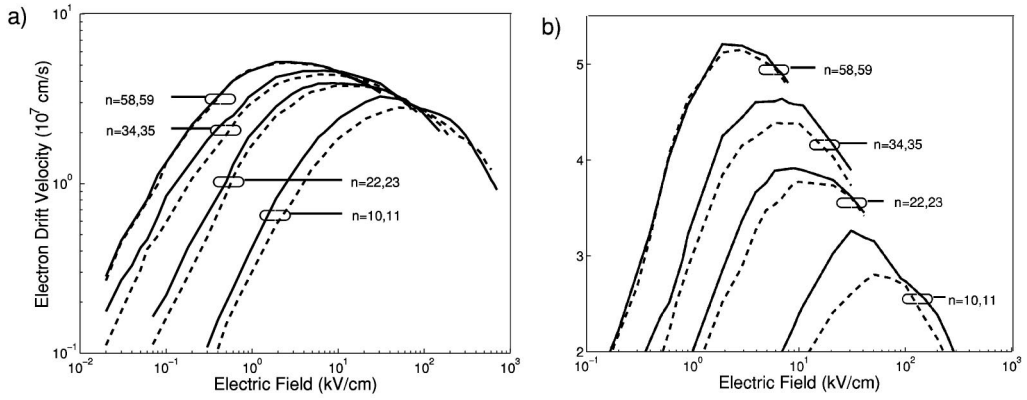

FIG. 7. Simulated drift velocity vs homogenous electric field for a number of zig-zag CNT's with indices n. Both the high and low field results are shown in (a), while (b) focuses on the peaks in the simulated drift velocity. Monte Carlo results are shown for type 1 tubes (- -), where $n+1$ is a multiple of 3, and for type 2 tubes (—), where $n-1$ is a multiple of 3. The variation in the drift velocity between the two tube types is significant only for the small tubes.

tering rate Γ which can be seen in Fig. 6. Between stochastically chosen scattering events during the simulation, electrons drift in the applied electric field. This drift time τ_d should be small compared to $1/\Gamma(E)$, so that the scattering rate is properly resolved in the Monte Carlo simulation. This requires that the drift time always be adjusted so that at all times $\tau_d(E) \leqslant 1/10\Gamma(E)$. For convergence in the low-field regime, where the electron mobility is constant, this criteria is adjusted so that $\tau_d(E) \leqslant 1/100\Gamma(E)$.

The simulated electron drift velocity, v_d, varies distinctly with applied electric field. Results are shown in Fig. 7 for fields where the average electron energy, which increases with increasing field, is below the bandstructure model limit of $5E_1^m(n)$. Peaks reaching values of v_d as large as $\cong 3-5 \times 10^7$ cm/s as n increases from 10 to 59 are observed. The critical field $F_c(n)$ at which the drift velocity maximum occurs is seen to decrease with increasing n from $\cong 60$ to 2 kV/cm in the range of n that is simulated. The low-field mobility is large, increasing as n, and thus the tube diameter, increases. This mobility increases from 0.4×10^4 to 12×10^4 cm^2/V/s as n increases from 10 to 59. Results for graphite, $\cong 1.5\times 10^4$ cm^2/V/s,[42] lie within this range. In the larger tubes, the low-field mobility is likely overestimated since electron-electron scattering is not considered. This is not the case in the smaller tubes since the phonon scattering rate is large and intersubband transitions at low fields are rare.

Negative differential mobility occurs when the slope of the drift velocity with field becomes negative. The simulated results show that dv_d/dF does indeed become negative once the velocity peak occurs. NDM is caused by the "transferred-electron effect"[43,44] involving the first two subbands. This occurs since the conduction velocity $(1/\hbar)(dE/dk)$ is larger in the first subband than in the second. The differential mobility becomes negative as the concentration of electrons in the second subband increases in response to an increasing applied electric field. For field-controlled NDM, the energy gap between the first two subbands should be large compared to the thermal energy of the electrons. This condition is met for the CNT's considered here, but for larger tubes this condition may not be satisfied.

Analysis of the dependence of the peaks in the drift velocity on the tube diameter and the bandstructure hopping integral γ, indicates a peak height of

$$v_d^{\max}(n) \cong 3\left(\frac{\gamma}{3}\right)^{2/3}\left[1+\frac{1-gcd(n+1,2)}{n}\right] \times \log_{10}(n)\times 10^7 \text{ cm/s}, \tag{27}$$

occurring at a critical field of

$$F_c(n) \cong \gcd(n+1,2)\left(\frac{\gamma}{3}\right)\left(\frac{1}{n}\right)^{3/2}\times 10^3 \text{ kV/cm}. \tag{28}$$

Differences based on the tube type are represented by the use of the greatest common divisor of $n+1$ and 2, $gcd(n+1,2)$. It is seen that the type 2 tubes have a drift velocity peak which is larger and a critical field which is half as large as in the type 1 tubes. This is illustrated in Fig. 7(b) where the peaks for both tube types are shown together. Since important features of charge transport occur at the critical field, Eq. (26) should be satisfied at this field value. We find that it is satisfied for the tubes considered. The band separation between the first and second subband satisfies Eq. (26) with at least a factor of 2.5 to spare in the tubes considered in this work. For increasing larger tubes though, the condition would eventually fail to be satisfied and field mediated intersubband transitions would occur readily.

One thing that determines the characteristics of the drift velocity peak is the decrease in the scattering rate with increasing n. As seen in Eq. (21), the scattering rates will be proportional to $D/\rho \propto \gamma/n^2$. With less scattering as n increases, electrons gain energy and occupy the second subband more readily as the field increases. This lowers the critical field significantly. The conduction velocity of the first subband, v_{c1}, also strongly influences the drift velocity. As n increases, this velocity increases weakly with n, allowing the electrons to reach higher drift velocities before the second subband is occupied. Differences in the peaks of v_d as the tube type varies result largely from alterations in v_{c1}. As

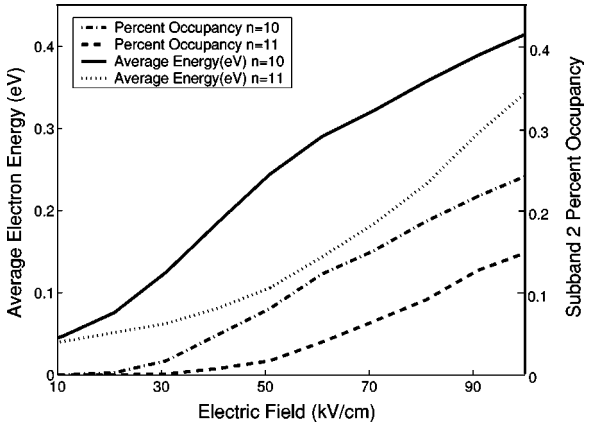

FIG. 8. Simulated average electron energy and percent occupancy of subband 2 vs electric field in a $n=10$ and a $n=11$ zig-zag CNT.

seen in Fig. 8, the average velocity and the occupation of the second subband both increase much faster with increasing field when $n=10$ as opposed to when $n=11$. This occurs since compared to the type 1 tubes, the effective mass of the type 2 tubes is smaller. Since the conduction velocity is proportional to $1/m_1^*(n)$, Table I shows that $v_{c1}(\vec{k},n)$ is larger in the type 2 tubes by a factor of $(n+4)/n$. For the large tubes considered this is a small increase, but for the smaller tubes this factor approaches 2. This leads to the deviations from Eqs. (27) and (28) for the different tube types that was mentioned earlier.

V. CONCLUSION

In summary, semiclassical transport has been applied to electron conduction through long ''perfect'' semiconducting zig-zag carbon nanotubes with wrapping indexes between 10 and 59. The zone-folding method is used to calculate the electronic energy levels consisting of two valleys, while scattering occurs through the interaction of electrons with the zone-folded longitudinally polarized acoustic phonon of graphene. Steady-state charge transport simulations considering a homogeneous applied electric field are performed using the Monte Carlo method.

Simulations at low fields show electron mobilities as large as in graphite for the larger tubes. At higher fields, the drift velocity is found to rise and peak with increasing field, reaching values as high as 5×10^7 cm/s in the larger tubes. It should be noted that the ability to extend the transport model to even larger zig-zag tubes in order to determine how these properties evolve further is limited by the decreasing energy spacing between the first two subbands. In larger tubes, the transport model must be altered if this spacing becomes small enough to allow field-assisted intersubband transitions or if the spacing approaches the thermal energy of the electrons.

The peaks in the electron drift velocity, which vary with *n*, show negative differential mobility due to electron transfer between the first two electronic subbands. This transfer may occur within the same or within different but equivalent bandstructure valleys. This effect also occurs in other traditional semiconductors with small direct bandgaps such as GaAs, but in these materials electron transfer between unequivalent valleys in the electronic bandstructure is usually involved. It is likely that some of the electronic properties of these materials may also exist in CNT's. One interesting property of GaAs related to NDM is its ability to support microwave fluctuations in the electron current know as the Gunn effect.[45] There are many applications of the NDM in these materials. Applications in electronics include use in oscillators, amplifiers, and logic and functional devices.[46] It may be possible that similar applications for CNT's may also exist.

[1] S. Iijima, Nature (London) **354**, 56 (1991).
[2] R. Saito, M.S. Dresselhaus, and G. Dresselhaus, in *Physical Properties of Carbon Nanotubes* (Imperial College Press, London, 1998).
[3] J. Li, C. Papadopoulos, and J.M. Xu, Nature (London) **402**, 253 (1999).
[4] W.Z. Li, J.G. Wen, and Z.F. Ren, Appl. Phys. Lett. **79**, 1879 (2001).
[5] R.S. Lee, H.J. Kim, J.E. Fischer, A. Thess, and R.E. Smalley, Nature (London) **388**, 255 (1997).
[6] L. Grigorian, G.U. Sumanasekera, A.L. Loper, S. Fang, J.L. Allen, and P.C. Eklund, Phys. Rev. B **58**, R4195 (1998).
[7] Z. Yao, C.L. Kane, and C. Dekker, Phys. Rev. Lett. **84**, 2941 (2000).
[8] J. Hone, M. Whitney, C. Piskoti, and A. Zettl, Phys. Rev. B **59**, R2514 (1999).
[9] A. Bachtold, P. Hadley, T. Nakanishi, and C. Dekker, Science **294**, 1317 (2001).
[10] R. Martel, T. Schmidt, H.R. Shea, T. Hertel, and Ph. Avouris, Appl. Phys. Lett. **73**, 2447 (1998).
[11] S.J. Tans, A.R.M. Verschueuren, and C. Dekker, Nature (London) **393**, 49 (1998).
[12] P.G. Collins, A. Zettl, H. Bando, A. Thess, and R.E. Smalley, Science **278**, 100 (1997).
[13] Z. Yao, H.W.C. Postma, L. Balents, and C. Dekker, Nature (London) **402**, 273 (1999).
[14] M.S. Fuhrer *et al.*, Science **288**, 494 (2000).
[15] C. Papadopoulos, A. Rakitin, J. Li, A.S. Vedeneev, and J.M. Xu, Phys. Rev. Lett. **85**, 3476 (2000).
[16] A.A. Odintsov, Phys. Rev. Lett. **85**, 150 (2000).
[17] F. Léonard and J. Tersoff, Phys. Rev. Lett. **85**, 4767 (2000).
[18] J. Kim, J. Lee, H. Oh, K. Yoo, and J. Kim, Phys. Rev. B **64**, 161404 (2001).
[19] S.L. Wang, N. Goldsman, Q. Lin, and J. Frey, Solid-State Electron. **36**, 833 (1993).
[20] C. Jacoboni and P. Lugli, in *The Monte Carlo Method for Semiconductor Device Simulation* (Springer-Verlag Wien, New York, 1989).
[21] M.V. Fischetti and S.E. Laux, Phys. Rev. B **38**, 9721 (1988).

[22] A. Spinelli, A. Benvenuti, and A. Pacelli, IEEE Trans. Electron Devices **45**, 1342 (1998).
[23] C.K. Huang and N. Goldsman, in *Proceedings of the 2001 International Conference on Simulation of Semiconductor Processes and Devices*, edited by D. Tsoukalas and C. Tsamis (Springer Wien, New York, 2001), p. 148.
[24] S.J. Tans, M.H. Devoret, H. Dai, A. Thess, R.E. Smalley, L.J. Geerligs, and C. Dekker, Nature (London) **386**, 474 (1997).
[25] J.W.G. Wildöer, L.C. Venema, A.G. Rinzler, R.E. Smalley, and C. Dekker, Nature (London) **391**, 59 (1998).
[26] T.W. Odom, J.L. Huang, P. Kim, and C.M. Lieber, Nature (London) **391**, 62 (1998).
[27] M. Ouyang, J.L. Huang, and C.M. Lieber, Phys. Rev. Lett. **88**, 066804 (2002).
[28] P.E. Lammert and V.H. Crespi, Phys. Rev. B **61**, 7308 (1998).
[29] D. Sánchez-Portal, E. Artacho, and J.M. Soler, Phys. Rev. B **59**, 12 678 (1999).
[30] G. Pennington and N. Goldsman, *2001 International Semiconductor Device Research Symposium* (IEEE, Piscataway, NJ, 2001), p. 310.
[31] M. Damnjanović, I. Milošević, T. Vuković, and R. Sredanović, Phys. Rev. B **60**, 2728 (1999).
[32] L. Yang, M.P. Anantram, J. Han, and J.P. Lu, Phys. Rev. B **60**, 13 874 (1999).
[33] R. Heyd, A. Charlier, and E. McRae, Phys. Rev. B **55**, 6820 (1997).
[34] M. Verissimo-Alves, R.B. Capaz, B. Koiller, E. Artacho, and H. Chacham, Phys. Rev. Lett. **86**, 3372 (2001).
[35] T. Hertel and G. Moos, Phys. Rev. Lett. **84**, 5002 (2000).
[36] B.K. Ridley, in *Quantum Processes in Semiconductors* (Oxford University Press, Oxford, 1982).
[37] L.J. Sham and J.M. Ziman, in *Solid State Physics*, edited by F. Seitz and D. Turnbull (Academic, New York, 1963), Vol. 15, p. 223.
[38] S. Briggs and J.P. Leburton, Phys. Rev. B **38**, 8163 (1988).
[39] S. Briggs, B.A. Mason, and J.P. Leburton, Phys. Rev. B **40**, 12 001 (1989).
[40] N. Ashcroft and N. Mermin, in *Solid State Physics* (Holt, Rinehart, and Winston, 1976).
[41] S. Briggs and J.P. Leburton, Phys. Rev. B **39**, 8025 (1989).
[42] D.E. Soule, Phys. Rev. **112**, 698 (1958).
[43] B.K. Ridley and T.B. Watkins, Proc. Phys. Soc. London **78**, 293 (1961).
[44] C. Hilsum, Proc. IRE **50**, 185 (1962).
[45] J.B. Gunn, Solid State Commun. **1**, 88 (1963).
[46] M. Shur, in *Physics of Semiconducting Devices* (Prentice-Hall, New Jersey, 1990).